Hindawi
Shock and Vibration
Volume 2020, Article ID 8811961, 16 pages
https://doi.org/10.1155/2020/8811961

*Research Article*

# Dynamic Model for Axial Motion of Horizontal Pelton Turbine and Validation in Actual Failure Case

**C. G. Rodriguez**,[1] **D. Zambrano**,[1] **S. Reyes**,[1] **J. Tapia**,[2] **M. Egusquiza**,[3] **and E. Egusquiza**[3]

[1]*Department of Mechanical Engineering, University of Concepcion, Edmundo Larenas 219, 4070409 Concepcion, Chile*
[2]*Department of Electrical Engineering, University of Concepcion, Edmundo Larenas 219, 4070409 Concepcion, Chile*
[3]*Centre of Industrial Diagnostics and Fluid Dynamics (CDIF), Technical University of Catalonia (UPC), Av. Diagonal 647, 08028 Barcelona, Spain*

Correspondence should be addressed to C. G. Rodriguez; cristian.rodriguez@udec.cl

Received 29 April 2020; Accepted 12 November 2020; Published 25 November 2020

Academic Editor: Paola Forte



Pelton turbines are important machines for power generation from a renewable energy source such as water. For power rates below 20 MW, the rotor of Pelton turbines is usually in horizontal position. Considering ideal mounting and operating conditions, there are no axial forces acting on the rotor. In practice, there is an hydraulic force due to the difference between nozzle centerline and bucket centerline, and there is a magnetic force due to the difference between axial position of stator and rotor magnetic field centers. These forces are supported by bearings. In this article, a nonlinear dynamic model considering these axial forces and bearings behavior is presented and solved for two different actual Pelton turbines. The nonlinear dynamic model allows determining and evaluating the source of axial motion and therefore provides valuable information in order to reduce it when the axial displacement is high enough to produce damage.

## 1. Introduction

Pelton turbines are widely used all over the world for electric power generation. This type of turbines with horizontal rotors is commonly used for power rates below 20 MW for small hydro power plant which allows environmentally friendly, local, and stable power supply.

There are several studies about the dynamic behavior of Pelton turbines and its failures. These studies are mainly focused on the performance calculation [1, 2]; the bucket erosion [3–6]; and the bucket fracture [7–9]. Computer fluid dynamics (CFD) simulations and most experimental studies are carried out considering that jet centerline coincides with bucket centerline. Taking into account this consideration, there are no axial forces and therefore there is no need to study the axial motion of horizontal Pelton turbines. However, in practice, it is found that, under some conditions, excessive axial motion can occur, producing, in some extreme cases, catastrophic failure of the bearing. The axial motion of an horizontal Pelton turbine is originated due to axial forces on the rotor, which can be originated due to two main causes (Figure 1):

(i) the axial force due to water jet on the bucket, $f_h$
(ii) the axial force due to the magnetic field on generator rotor, $f_m$.

Axial force on the bucket due to water jet is zero if the jet centerline coincides with bucket centerline. If both centerlines do not coincide, then there will be an axial force $f_h$ due to uneven separation of water jet as schematically shown in Figure 2. Another axial force is due to the magnetic force on the rotor generator. This force should be zero if the axial position of the stator magnetic field center coincides with the axial position of rotor magnetic field center. If both axial positions do not coincide, then there will be an axial force $f_m$ on the rotor as schematically shown in Figure 3. These

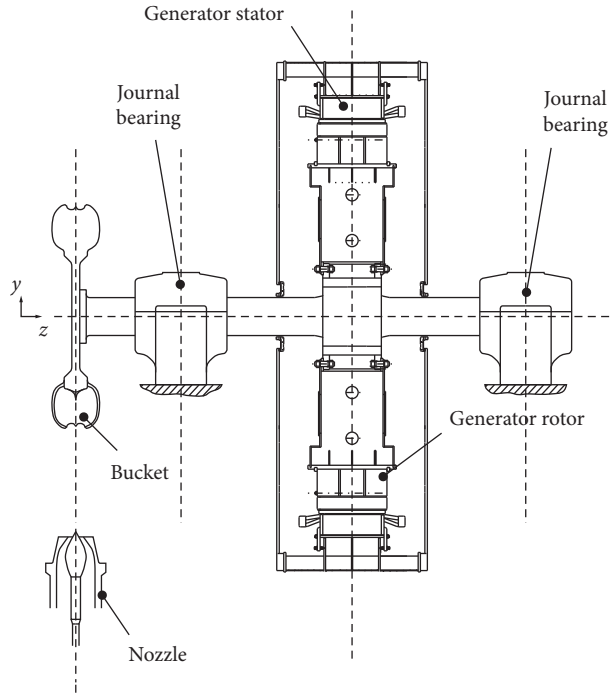


Figure 1: Horizontal Pelton turbine.

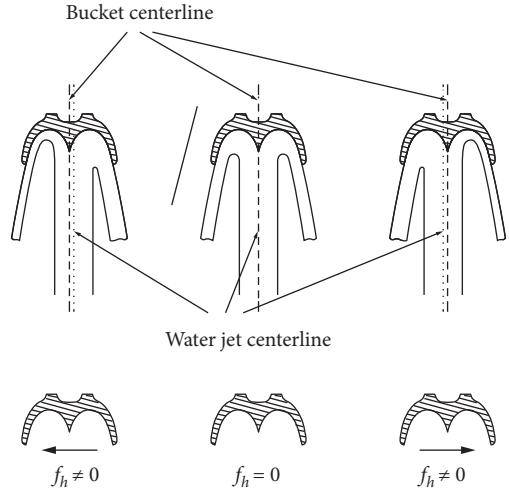


Figure 2: Force on bucket due to the difference between water jet centerline and bucket centerline.

undesirable resultant axial forces on the rotor are supported by bearing reaction which can be degraded over the time. In the following study, a model for axial motion considering these forces will be presented and then it will be used in two actual cases of horizontal Pelton turbines: one in normal operating condition and another presenting excessive axial motion with bearing failure as a consequence.

## 2. The Model

*2.1. Axial Force on the Bucket due to Water Jet.* To determine the axial force generated by water jet on the bucket, let us consider that the centerlines of the jet and bucket are parallel but displaced from each other by a distance $z - z_{n0}$, where $z$ is the moving axial position of bucket plane and $z_{n0}$ is the fixed axial position of nozzle centerline. Considering the diameter of water jet as $d$ and that the jet is separated by bucket cut-out at $z$, then the amount of flow rate in each side of bucket exit will be $Q_L$ at the left and $Q_R$ at the right, as shown in Figure 4.

Figure 5 shows the jet separation where $\theta$ is the angle of intersection between water jet diameter and bucket cut-out that is given by $\theta = 2\cos^{-1}(2(z - z_{n0})/d)$. Considering that $v$ is the mean inlet relative velocity of water into bucket, then $Q_L$ and $Q_R$ are determined by the following equation:

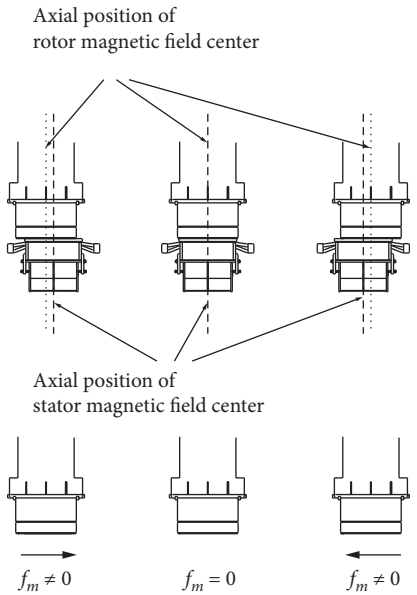


Figure 3: Force on rotor due to the difference between axial position of stator and rotor magnetic field centers.

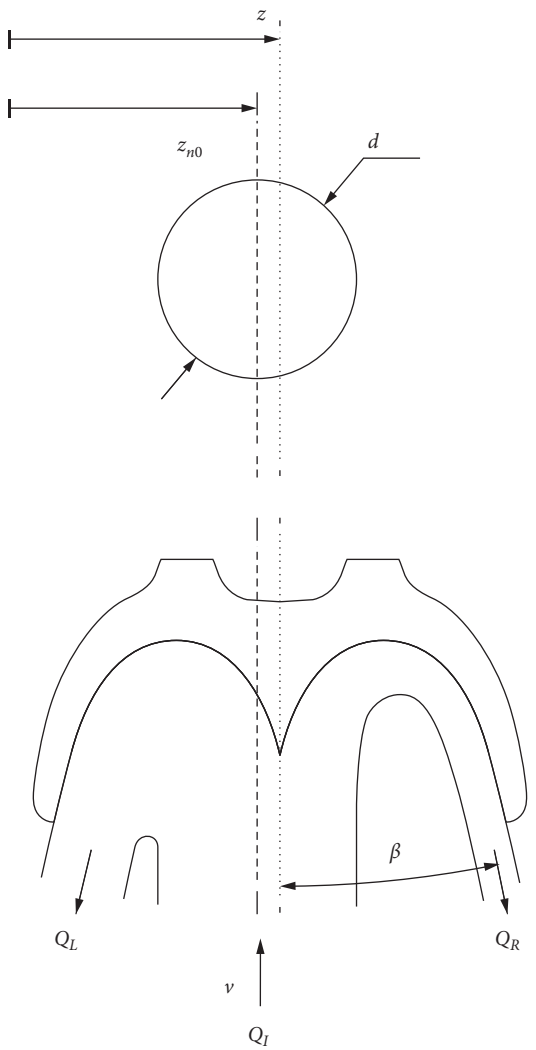


Figure 4: Uneven separation of water jet in Pelton turbine bucket.

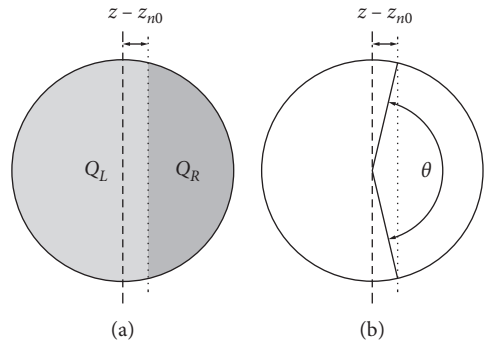


Figure 5: Geometry of water jet separation in bucket.

$$Q_L = v\left(\frac{\pi d^2}{4} - \frac{\theta d^2}{8} + \frac{(z - z_{n0})d}{2}\sin\frac{\theta}{2}\right),$$
$$Q_R = v\left(\frac{\theta d^2}{8} - \frac{(z - z_{n0})d}{2}\sin\frac{\theta}{2}\right). \quad (1)$$

Then, the axial force on bucket due to change in momentum can be determined as follows:

$$f_h = \frac{1}{4}\rho v^2 d^2 \sin\beta\left(\pi - 2\cos^{-1}\frac{2(z - z_{n0})}{d} + 4\left(\frac{z - z_{n0}}{d}\right)\cdot\sin\left(\cos^{-1}\frac{2(z - z_{n0})}{d}\right)\right). \quad (2)$$

In equation (2), $\rho$ is the water density and $\beta$ is the angle of water exit.

The axial hydraulic force $f_h$ in equation (2) is shown in Figure 6. It can be observed that for a positive displacement in $z - z_{n0}$, there will be a force on the bucket in the same direction. This behavior is equivalent to a negative stiffness giving instability to axial rotor position.

The bucket's relative position with respect to jet impact position changes as rotor rotates (Figure 7); thus, there is a variation of force magnitude every time a bucket passes, which leads into a magnitude variation at the bucket passing frequency $Z_B\,\Omega$, with $Z_B$ being the number of buckets and $\Omega$ the rotating speed. This amplitude modulation is incorporated to the model using the modulation function $A_h$ in equation (3). The shape of modulation function is based on CFD results of force and torque variation due to rotation as [10] (solid line in Figure 8 for single bucket as rotor rotates). The experimental data of [11] shows the same behavior but with a short duration peak when the bucket is first reached by jet (dashed line in Figure 8). The existence of this peak is not explained with CFD simulations and it is supposed to be originated in the way pressure is measured [12–14]. This peak in the modulation function would produce several harmonics of blade passing frequency. During prototype measurements, it is found that there are no high harmonics of bucket passing frequency ($>5Z_B\Omega$) in axial motion; therefore, peak consideration does not provide significant difference in axial calculated motion, and for that reason, the modulation function considers the first four harmonics of blade passing frequency ($Z_B\Omega, 2Z_B\Omega, 3Z_B, \Omega$ and $4Z_B\Omega$).

$$A_h = 1 + \sum_{n=1}^{4} a_{hn}\cos nZ_B\Omega t + \sum_{n=1}^{4} b_{hn}\sin nZ_B\Omega t. \quad (3)$$

In equation (3), $a_{hn}$ and $b_{hn}$ are the Fourier coefficients that are calculated to describe the hydraulic force modulation function (obtained from Figure 8 repeated for each bucket). After these considerations, the axial force on the buckets is obtained as follows:

$$f_h = \left[\frac{1}{4}\rho v^2 d^2 \sin\beta\left(\pi - 2\cos^{-1}\frac{2(z - z_{n0})}{d} + 4\left(\frac{z - z_{n0}}{d}\right)\sin\left(\cos^{-1}\frac{2(z - z_{n0})}{d}\right)\right)\right] * \left[1 + \sum_{n=1}^{4} a_{hn}\cos nZ_B\Omega t + \sum_{n=1}^{4} b_{hn}\sin nZ_B\Omega t\right]. \quad (4)$$

*2.2. Axial Force on the Rotor Generator due to Magnetic Forces.* Magnetic fields in stator and rotor generator can be considered as symmetrical with respect to an axial position in both stator and rotor. The axial position of stator magnetic field center is fixed, while the axial position of rotor magnetic field center moves with the rotor. If both axial positions do

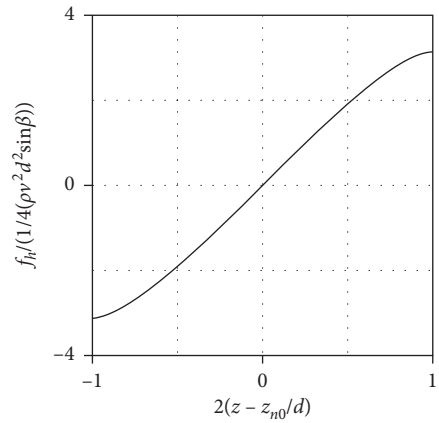


Figure 6: Axial force on the bucket due to difference between nozzle and bucket centerlines.

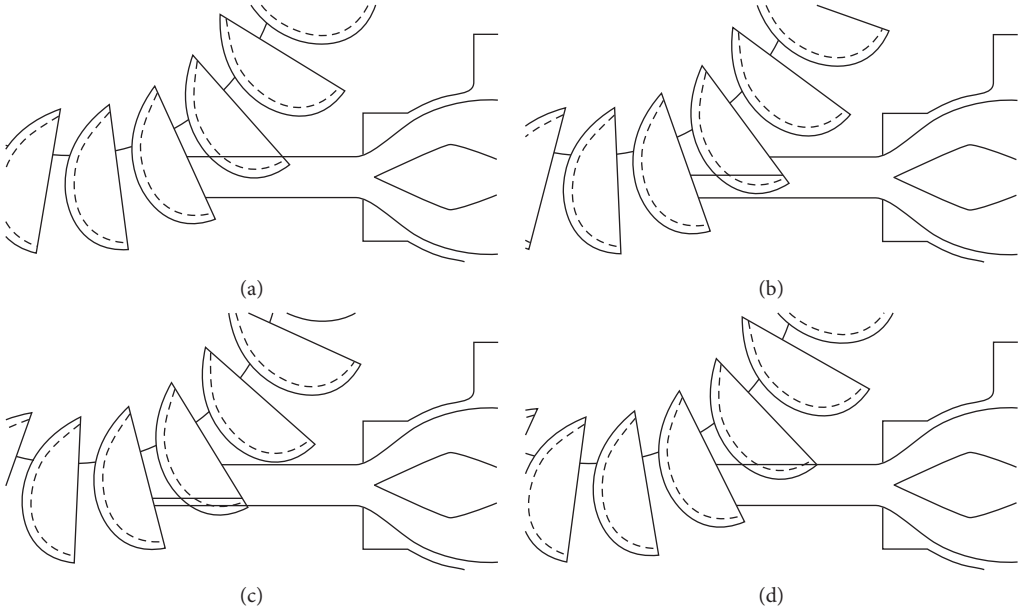


Figure 7: Bucket relative position to water jet.

not coincide, then there will be a magnetic force or magnetic pull that tries to maintain both magnetic fields centers at the same axial position.

Figure 9 shows the axial rotor magnetic field center at $z + z_{rs}$ that does not coincide with axial position of stator magnetic field center which is at $z_{s0}$, with $z_{rs}$ being the axial distance between bucket centerline and rotor magnetic field center. The axial distance between both magnetic centers is $z + z_{rs} - z_{s0}$. The diameter of stator is $d_s$, and the diameter of rotor is $d_r$.

The magnetic force on rotor due to interaction of the $Z_p$ poles as a consequence of different axial position is given by the following equation [15]:

$$f_m = -\frac{1}{2} i^2 N^2 Z_p \frac{\partial \mathscr{P}(z)}{\partial z}. \tag{5}$$

In equation (5), $i$ is the current, $N$ is the number of turns, and $\mathscr{P}$ is the permeance. Permeance is given by the following equation:

$$\mathscr{P} = \mathscr{P}_1 + \mathscr{P}_2. \tag{6}$$

In equation (6), $\mathscr{P}_1$ and $\mathscr{P}_2$ are the permeances of the two parts in the generator air gap as shown in Figure 10, which are given by the following equations, where $\mu_0$ is the magnetic permeability of air.

$$\mathscr{P}_1 = \pi \mu_0 \frac{(d_s + d_r)\left(L - \left|z + z_{rs} - z_{s0}\right|\right)}{d_s - d_r}, \tag{7}$$

$$\mathscr{P}_2 = \mu_0 (d_s + d_r) \ln\left(1 + \pi \frac{\left|z + z_{rs} - z_{s0}\right|}{d_s - d_r}\right). \tag{8}$$

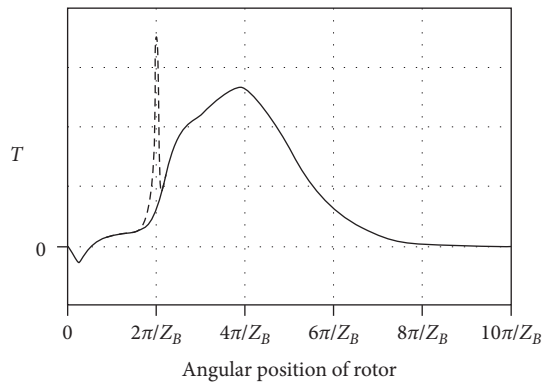


Figure 8: Torque as a function of angular position due to one bucket from CFD calculation and experiments (schematically from [11, 14]).

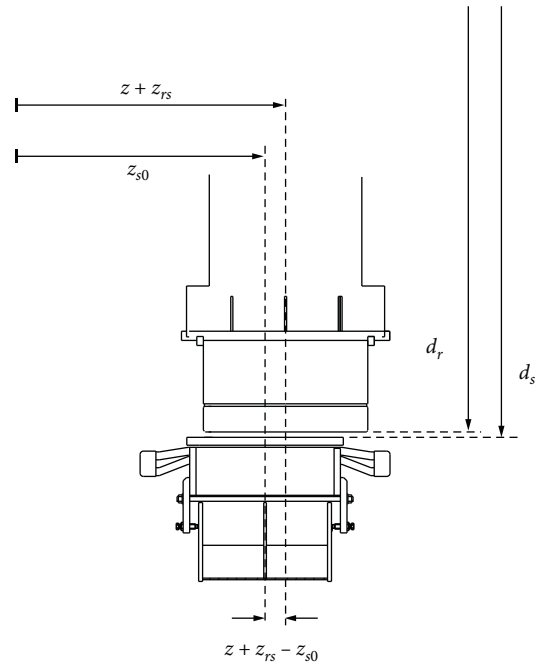


Figure 9: Axial position of stator and rotor magnetic field centers.

Using equations (6) to (8) into (5), the axial magnetic force in equation (9) is obtained. Figure 11 shows magnetic force magnitude considering typical values of $d_s$, $d_r$, and $L$ for a 1000 rev/min and 10 MW generator. References [16–18] obtain a similar behavior for axial force.

$$f_m = -\frac{1}{2}\mu_0 \pi^2 i^2 Z_p N^2 \frac{(d_s + d_r)}{(d_s - d_r)} \frac{z + z_{rs} - z_{s0}}{\left[(d_s - d_r) + \pi\left|z + z_{rs} - z_{s0}\right|\right]}. \quad (9)$$

As in the case of axial force due to jet, there will be a change in the magnitude of the magnetic force as rotor rotates due to relative position of poles. This change in magnetic force will be considered as the modulation function $A_m$ in equation (10) at twice pole passing frequency ($2Z_P\Omega$, $Z_P$ being the number of poles). The shape of modulation function shown in Figure 12 is taken from electrical simulations of magnetic pull during rotation as [19]. The modulation function considers the first four harmonics of twice pole passing frequency ($2Z_P\Omega, 4Z_P\Omega, 6Z_P\Omega$, and $8Z_P\Omega$).

$$A_m = 1 + \sum_{n=1}^{4} a_{mn} \cos 2nZ_P\Omega t + \sum_{n=1}^{4} b_{mn} \sin 2nZ_P\Omega t. \quad (10)$$

In equation (10), $a_{mn}$ and $b_{mn}$ are the Fourier coefficients that are calculated to describe time waveform of magnetic force modulation function in Figure 12.

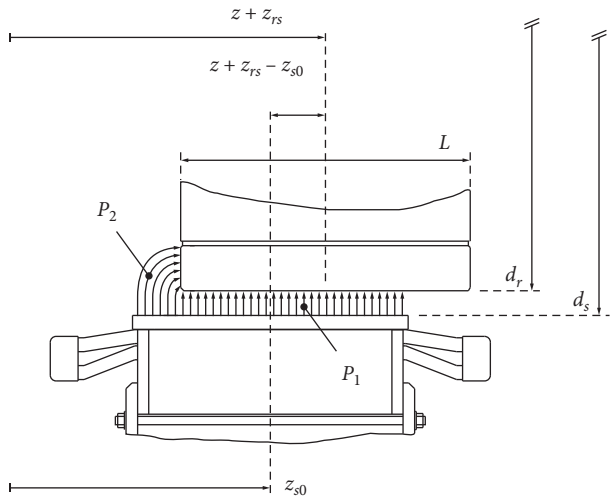


Figure 10: Axial magnetic force calculation.

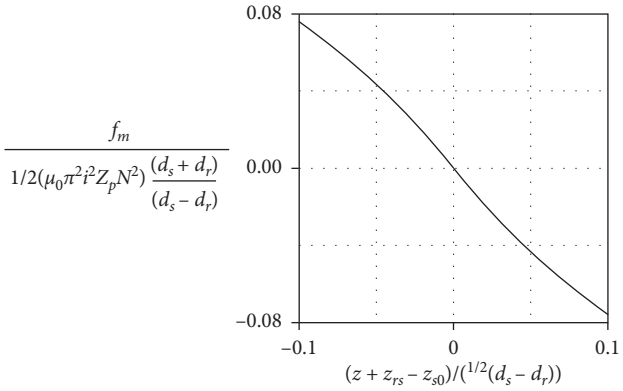


Figure 11: Axial force magnitude on rotor generator.

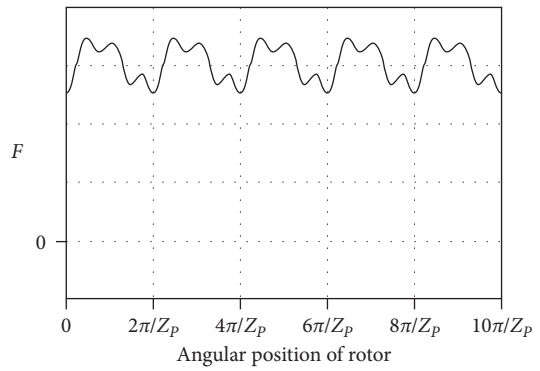


Figure 12: Shape of magnetic force (schematically from Kang et al., 2017).

After these considerations, the axial magnetic force on rotor is given by

$$f_m = -\frac{1}{2}\mu_0\pi^2 i^2 Z_p N^2 \frac{(d_s + d_r)}{(d_s - d_r)} \frac{z + z_{rs} - z_{s0}}{\left[(d_s - d_r) + \pi\left|z + z_{rs} - z_{s0}\right|\right]} * \left[1 + \sum_{n=1}^{4} a_{mn}\cos 2nZ_P\Omega t + \sum_{n=1}^{4} b_{mn}\sin 2nZ_P\Omega t\right]. \quad (11)$$

*2.3. Axial Reaction Force on Bearing.* The bearings are usually two and are mounted with the rotor centered by the nozzle centerline and bucket centerline at the same position. One of the bearings will be mounted in order to support axial motion in one direction and the other bearing will be mounted in order to support axial motion in the other axial direction. In each one of the bearings, there will be a working side and a nonworking side. The working side in each bearing is obtained giving an adequate axial clearance to form lubricant film between rotor and bearing surfaces as shown in Figure 13. In some turbine designs, a single bearing has both working sides.

If the clearance in the working side is higher than the one necessary to obtain an adequate lubricant behavior, then there will be an interval of axial motion $\Delta z_{b0}$ where the bearing is not able to provide a reaction force. To incorporate this condition to model, a zero stiffness interval is incorporated to bearing behavior. If the clearance in the working side is necessary to obtain an adequate lubricant behavior, then the bearing behaves as a constant stiffness spring. To incorporate this condition to model, a stiffness of $k_1$ is incorporated to bearing behavior. The value of $k_1$ is obtained making use of bearing geometry and the calculations based on [20]. If the clearance in the working side is lower than the one necessary to obtain an adequate lubricant behavior, then there is a high axial force (in comparison to the one considered by design) and bearing could be damaged. To incorporate this condition to model, a high stiffness $k_2$ is incorporated to bearing behavior. This behavior is equivalent to a single bearing with maximum displacement of shaft in axial direction $l_b = l_2 - l_1$ centered at an axial distance $z_{b0}$ which is schematically shown in Figures 14 and 15.

Taking the previous analysis into account, the bearing axial stiffness is considered as follows:

$$k_b = \begin{cases} 0 \quad \text{if } \left|z + z_{rb} - z_{b0}\right| < \dfrac{\Delta z_{b0}}{2}, \\ k_1, \quad \text{if } \Delta z_b \le \left|z + z_{rb} - z_{b0}\right| < \dfrac{l_b}{2}, \\ k_2 = \infty, \quad \text{if } \left|z + z_{rb} - z_{b0}\right| \ge \dfrac{l_b}{2}. \end{cases} \tag{12}$$

In equation (12), $z_{rb}$ is the distance between bucket plane and axial position of bearing in rotor. To take into account the bearing stiffness, it is not necessary to add a modulation function because bearings are flat, and no significant variation of stiffness is found in a single rotation of rotor.

*2.4. Equation of Motion.* Due to high torque and low rotating speed in hydraulic turbines, the rotor has a higher diameter in relation to its length when compared to other types of turbines as gas or steam turbines. For that reason, the rotor first natural frequency in flexion is usually much higher than its rotating speed. Moreover, the first natural frequency in axial compression and traction is much higher than the first natural frequency in flexion. For these reasons, the rotor is considered as a rigid body in axial direction. Simulations of horizontal Pelton turbines [21] show that axial natural frequencies are much higher than those of excitation forces. By international standards as API 670, the rotor should be considered as a rigid body if its main excitation frequency is below 0.7 times rotor natural frequency. In the case of the proposed model, the excitation in axial direction with higher frequency is the bucket passing frequency ($Z_B\Omega$) which must be lower than 0.7 times its first axial natural frequency ($f_{n,a}$) to be considered as rigid. For the simulated cases, this condition is verified before computing the model that is represented by

$$\sum f = m\ddot{z}, \quad f_h + f_m - k_b z + z_{rb} - z_{b0} - c_b\dot{z} = m\ddot{z}. \tag{13}$$

In equation (13), $m$ is rotor mass, and $c_b$ is an introduced bearing damping, considered in order to eliminate initial transient response. Considering the previous axial forces and bearing axial stiffness, the model equation of motion is given by equation (14) and schematically shown in Figure 16.

$$\begin{aligned} &\left\{\left[\frac{1}{4}\rho v^2 d^2 \sin\beta\left(\pi - 2\cos^{-1}\frac{2(z - z_{n0})}{d} + 4\left(\frac{z - z_{n0}}{d}\right)\sin\left(\cos^{-1}\frac{2(z - z_{n0})}{d}\right)\right)\right]\right. \\ &\left.* \left[1 + \sum_{n=1}^{4} a_{hn}\cos nZ_B\Omega t + \sum_{n=1}^{4} b_{hn}\sin nZ_B\Omega t\right]\right\} \\ &+ \left\{-\frac{1}{2}\mu_0\pi^2 i^2 Z_p N^2 \frac{(d_s + d_r)}{(d_s - d_r)} \frac{z + z_{rs} - z_{s0}}{\left[(d_s - d_r) + \pi\left|z + z_{rs} - z_{s0}\right|\right]} * \left[1 + \sum_{n=1}^{4} a_{mn}\cos nZ_P\Omega t + \sum_{n=1}^{4} b_{mn}\sin nZ_P\Omega t\right]\right\} \\ &- k_b(z + z_{rb} - z_{b0}) - c_b\dot{z} = m\ddot{z}. \end{aligned} \tag{14}$$

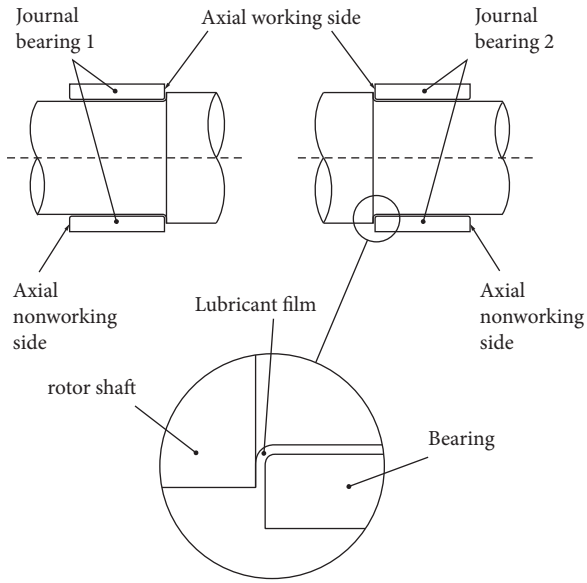


Figure 13: Axial working and nonworking side of two bearings.

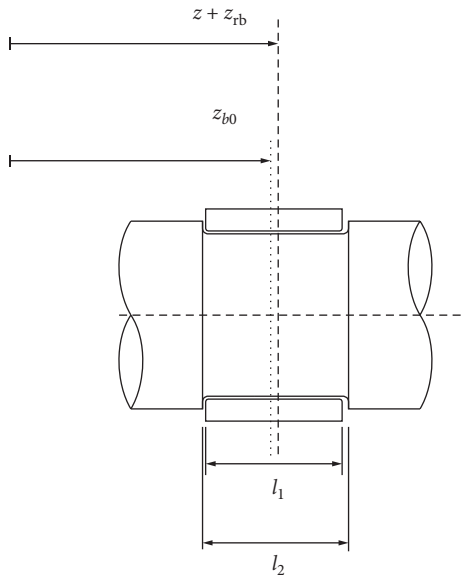


Figure 14: Equivalent bearing.

In Figure 16, the conditions that are important for adequate axial behavior are as follows:

(i) The positions for zero axial force are equal for $f_h$ and $f_m$, which means that $z_{s0} - z_{n0} = z_{rs}$

(ii) The position for zero axial forces coincides with the axial position of zero reaction at bearing, which means that $z_{b0} - z_{n0} = z_{rb}$

(iii) Axial clearance of bearing is adequate

The nonlinear differential equation of motion in equation (14) was solved making use of MATLAB, using ode113 with a variable time step.

*2.5. Model Variables to be Determined.* Rotor dimensions, rotor material, flow rate, power rate, and generator current and voltage are known. Then, the model can be solved for different values of $z_{n0}, z_{b0}, z_{s0}, z_{rb}, z_{rs}, \Delta z_{b0}$, and $l_b$. These values are adjusted in order to obtain an axial behavior similar to the actual axial behavior.

The value $z_{n0} = 0$ is considered in simulations as the reference for axial position. For the first simulation for adjustment, it was considered that (i) the distance $z_{rb}$ is equal to the distance between bucket centerline and the axial position of bearing center $Z_{rb}$ determined by turbine specifications; (ii) the distance $z_{rs}$ is equal to the distance between bucket centerline and the axial position of generator

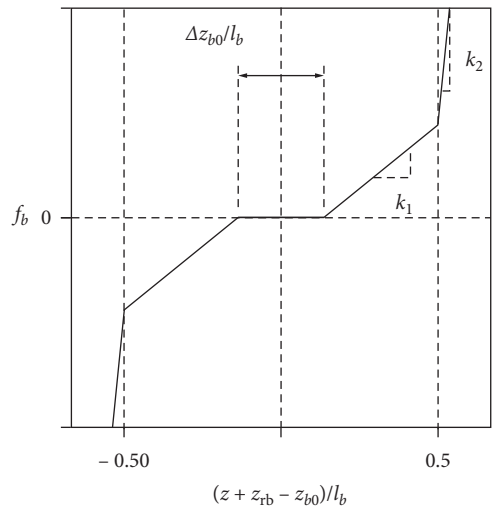


Figure 15: Bearing axial stiffness.

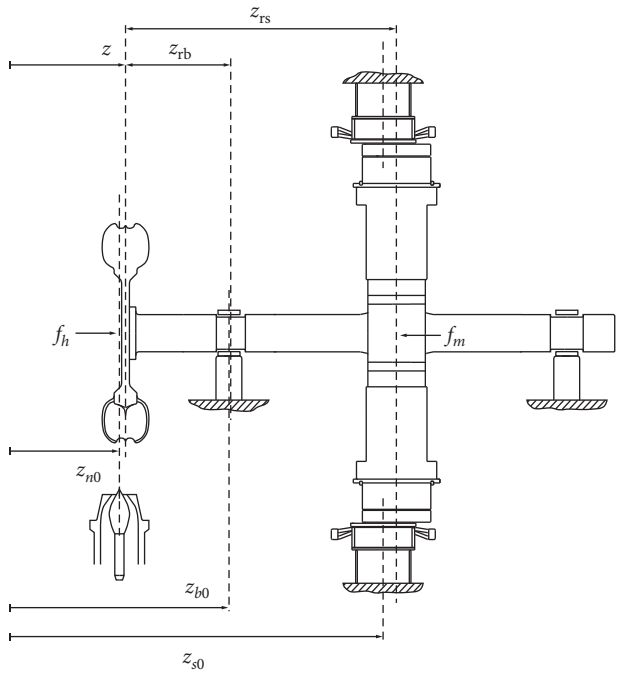


Figure 16: Model of Pelton turbine axial motion.

rotor geometric center $Z_{rs}$ determined by turbine specifications; and (iii) $\Delta z_{b0}$ is considered as zero which means that the axial clearance is supposed to be equal or lower than the one necessary to obtain an adequate lubricant film behavior. Taking into account these considerations for the first simulation, then the values of $z_{s0}$, $z_{b0}$, and $l_b$ are determined. If these values cannot provide a good agreement of model to experimental data, then the values of $z_{rb}, z_{rs}$, and $\Delta z_{b0}$ are modified and adjusted. After this, the modulation functions for hydraulic and magnetic forces are modified until the best agreement with measurements is obtained. This procedure is schematically shown in Figure 17.

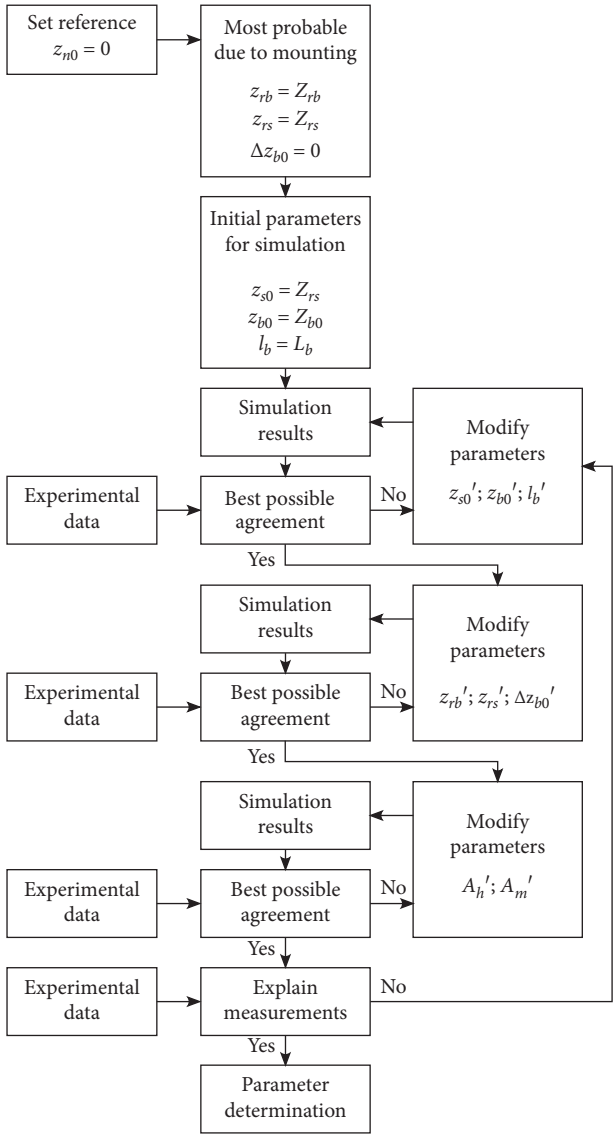


Figure 17: Adjustment of model parameters.

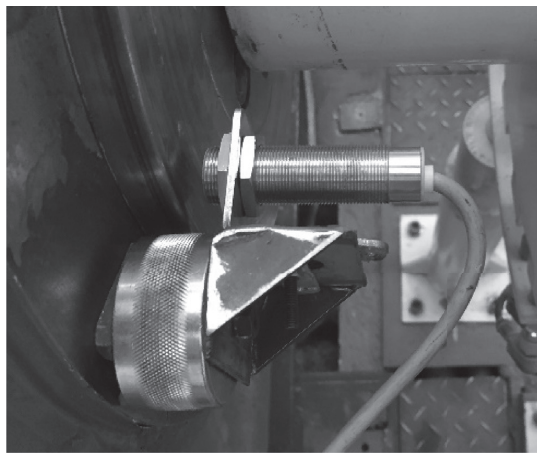

Figure 18: Axial movement measurement.

Table 1: Horizontal Pelton turbine, Case I.

| | | |
|---|---|---|
| Power rate | 10 | MW |
| Net head | 600 | m |
| Flow | 1.89 | $m^3/s$ |
| Number of buckets | 19 | |
| Rotating speed | 1000 | rpm |
| Rotor length | 1.240 | m |
| Rotor diameter | 1.480 | m |
| Stator diameter | 1.500 | m |
| Total rotor weight | 11800 | kg |
| Number of poles | 6 | |

Table 2: Calculated parameters, Case I.

| | | |
|---|---|---|
| $z_{rs} - (z_{s0} - z_{n0})$ | 1.70 | mm |
| $z_{rb} - (z_{b0} - z_{n0})$ | −0.30 | mm |
| $\Delta z_{b0}$ | 0.00 | mm |
| $l_b$ | 0.90 | mm |
| Máx $(a_{hn}, b_{hn})$ | 0.00 | |
| Máx $(a_{mn}, b_{mn})$ | 0.00 | |

The adjustment was carried out making use of different measurements of turbine. It is useful to count on the axial motion measured rotating at constant speed, zero current, and zero voltage in generator: full speed no load (FSNL). This condition allows focusing on $z_{b0}$ and $l_b$ because there is not magnetic force on rotor at this operating condition. Then, it is necessary to count on the axial motion measured at different power in order to focus on $z_{s0}$.

## 3. Actual Cases

*3.1. Measurements.* Measurements were carried out in two different power stations. In both stations, power rate, stator and rotor currents and voltages, and nozzle spear position were obtained from power station control system. Axial motion was measured making use of displacement sensor Baumer IWRM 18U9501 with a measuring range from 2 to 5 mm mounted in a support with a magnetic ferrite base (Figure 18). The displacement sensor was powered by a 24 V power supply. The rotating speed was determined using the voltage output of a Monarch PLT200 optical tachometer which detected a reflective tape in rotor using a laser light source. The voltage signal from displacement sensor and optical tachometer was recorded using a NI 9229 module installed in a CompactDAQ 9174 USB chassis both from National Instruments. The analog to digital converter of NI 9229 allowed measuring a voltage range of ±60 V at 24 bits. The sampling frequency used in measurements was 25600 Hz.

*3.2. Case I: Actual Case with Normal Axial Motion.* The first actual case, using the model, considers the Pelton turbine described in Table 1. This unit was operating for twenty-two months presenting no bearing failure and normal working temperatures. After parameter adjustment, the values of axial position of stator and rotor magnetic field centers, bearing center, bearing axial clearance, and bearing nonworking interval are shown in Table 2. Figure 19 shows the waveform of model prediction and measurements at different operating conditions. Table 3 shows the maximum, minimum, and averaged axial position obtained with model predictions and measurements. A good agreement is observed between simulated and measured axial motion.

After this analysis, and taking into account the values in Table 2, it was concluded that the axial motion was normal and adequate for continuous operation with no restrictions.

*3.3. Case II: Actual Case with Excessive Axial Motion and Bearing Failure.* The second actual case, using the model, considers the Pelton turbine described in Table 4. The stator poles of this Pelton turbine were replaced due to the end of its useful life. After startup, there was a bearing failure, showing Babbitt erosion and contact in axial direction. After this failure, bearing was repaired and mounted. The measurements shown in this section were taken after reparation. After parameter adjustment, the values of axial position of stator and rotor magnetic field centers, bearing center, bearing axial clearance, and bearing nonworking interval are shown in Table 5. Figure 20 shows the waveform of model prediction and measurements at different operating conditions. Table 6 shows the maximum, minimum, and averaged axial position obtained with model predictions and

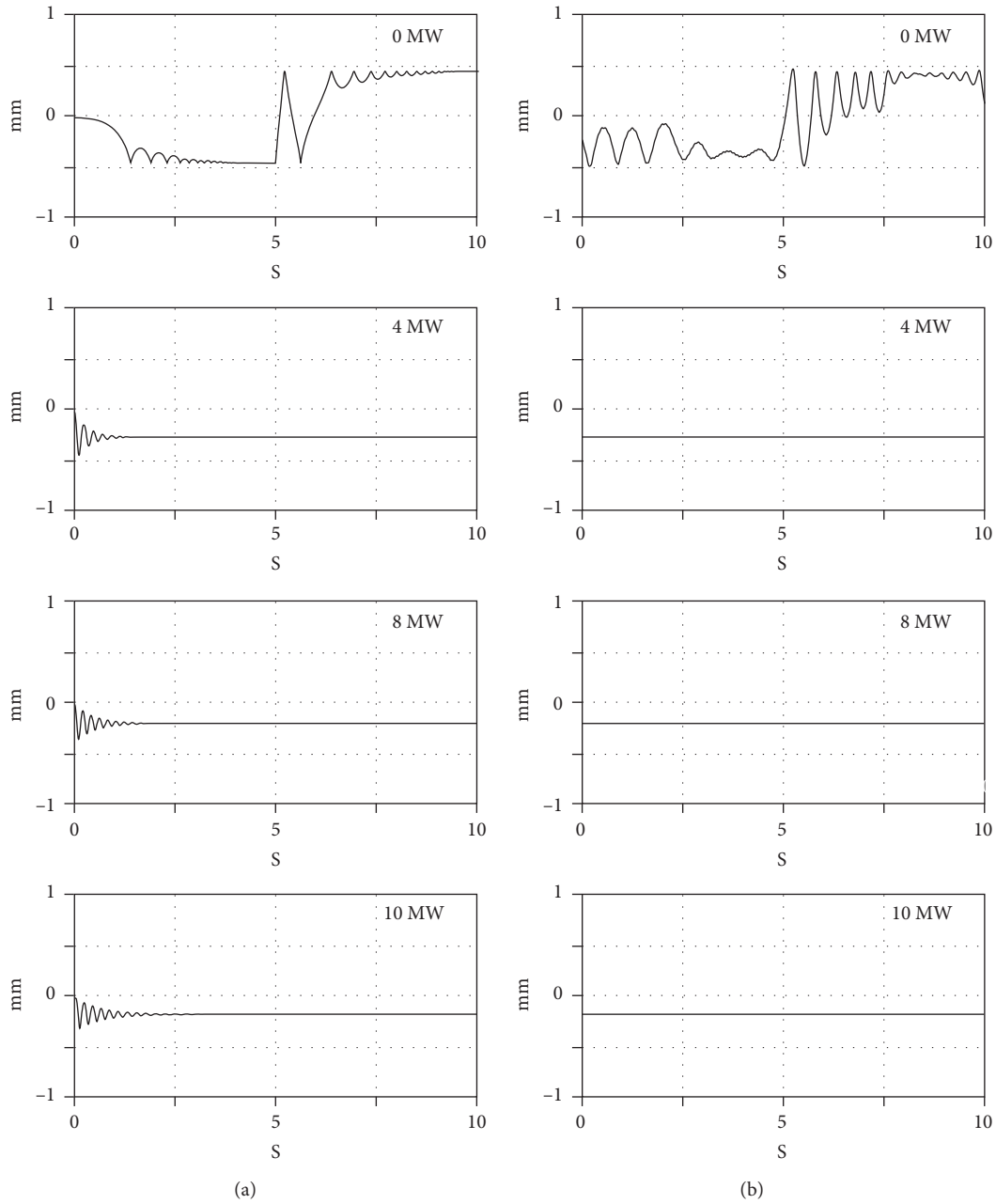


Figure 19: Simulated and measured waveform, Case I. (a) Simulation. (b) Experimental.

Table 3: Model prediction and experimental measurements, Case I.

| Power rate in MW | | Axial position of rotor in mm | | |
|---|---|---|---|---|
| | | Model prediction | Experimental measurement | Difference |
| 0 | Maximum | 0.45 | 0.45 | 0.00 |
| | Minimum | −0.45 | −0.45 | 0.00 |
| 2 | Maximum | −0.27 | −0.28 | 0.01 |
| | Minimum | −0.29 | −0.28 | 0.01 |
| 4 | Maximum | −0.25 | −0.26 | 0.01 |
| | Minimum | −0.26 | −0.26 | 0.00 |
| 6 | Maximum | −0.22 | −0.23 | 0.01 |
| | Minimum | −0.23 | −0.23 | 0.00 |
| 8 | Maximum | −0.19 | −0.20 | 0.01 |
| | Minimum | −0.20 | −0.20 | 0.00 |
| 10 | Maximum | −0.17 | −0.17 | 0.00 |
| | Minimum | −0.18 | −0.17 | 0.01 |

Table 4: Horizontal Pelton turbine, Case II.

| | | |
|---|---|---|
| Power rate | 8 | MW |
| Net head | 475 | m |
| Flow | 1.91 | $m^3/s$ |
| Number of buckets | 19 | |
| Rotating speed | 300 | rpm |
| Rotor length | 0.500 | m |
| Rotor diameter | 3.330 | m |
| Stator diameter | 3.460 | m |
| Total rotor weight | 20800 | kg |
| Number of poles | 20 | |

Table 5: Calculated parameters, Case II.

| | | |
|---|---|---|
| $z_{rs} - (z_{s0} - z_{n0})$ | 9.65 | mm |
| $z_{rb} - (z_{b0} - z_{n0})$ | 10.28 | mm |
| $\Delta z_{b0}$ | 0.00 | mm |
| $l_b$ | 0.80 | mm |
| Máx$(a_{hn}, b_{hn})$ | 0.00 | |
| Máx$(a_{mn}, b_{mn})$ | 0.00 | |

Table 6: Model prediction and experimental measurements, Case II.

| Power rate in MW | | Axial position of rotor in mm | | |
|---|---|---|---|---|
| | | Model prediction | Experimental measurement | Difference |
| 2 | Maximum | 0.04 | 0.03 | 0.01 |
| | Minimum | 0.03 | 0.03 | 0.00 |
| 4 | Maximum | 0.18 | 0.18 | 0.00 |
| | Minimum | 0.17 | 0.18 | 0.01 |
| 6 | Maximum | 0.30 | 0.30 | 0.00 |
| | Minimum | −0.50 | −0.50 | 0.00 |
| 8 | Maximum | 0.30 | 0.30 | 0.00 |
| | Minimum | −0.50 | −0.50 | 0.00 |

measurements. A good agreement is observed between simulated and measured axial motion.

In this case, there was a nonstationary behavior for power rates over 6 MW. Over 6 MW, there is an axial bounce of rotor against bearing. After this analysis, and taking into account the values in Table 5, it was concluded that the axial motion was mainly due to the difference between axial position of stator and rotor magnetic field centers and due to the difference between axial positions of bearing. Until corrective action, it was suggested not to operate over 4 MW. A corrective action was performed moving bearing in order to correct axial position. It was not considered to move stator frame or to move nozzle because it is more expensive in time and costs when comparing to bearing adjustment. After this correction, no bounces in axial motion were detected at 6 and 8 MW, and the unit was able to operate at all its power ranges.

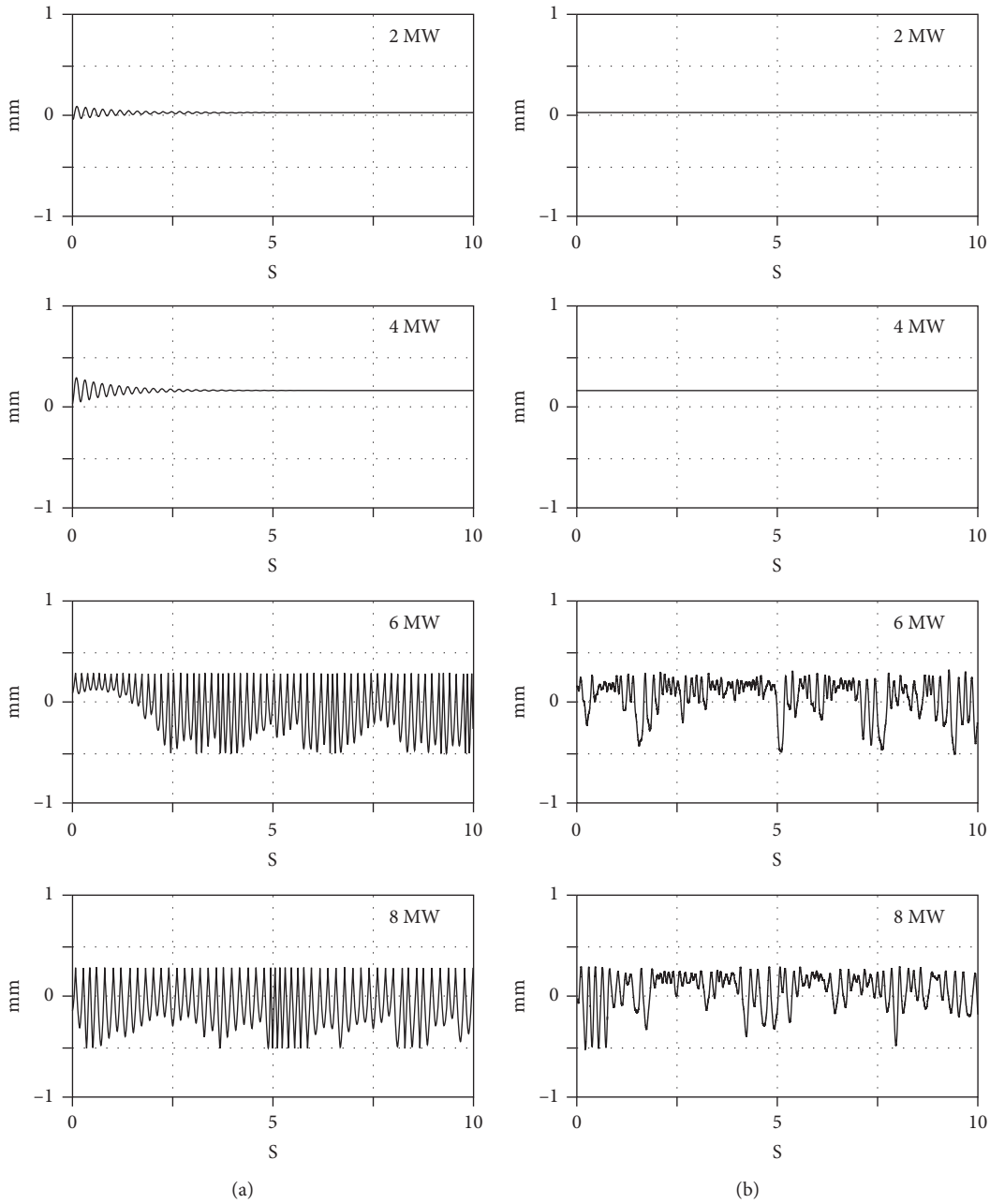


Figure 20: Simulated and measured waveform, Case II. (a) Simulation. (b) Experimental.

## 4. Conclusions

A model of axial motion of Pelton horizontal turbine is proposed. The model needs a set of experimental data under different operating conditions in order to determine the unknown values of axial position of stator and rotor magnetic field centers, bearing position, and bearing clearance. After the adjustment of these variables, the model accurately predicts axial motion of Pelton horizontal turbine. Knowing these variables allows evaluating the influence of different sources of axial motion: due to the difference in centerlines of nozzle and bucket and due to the difference in axial position of stator and rotor magnetic field centers; due to bearing positioning and due to bearing axial clearance.

The model is tested in two cases: with a turbine under normal axial motion and with a turbine presenting excessive axial motion and damage in one of the bearings. In the case of excessive axial motion, it was possible to determine the main causes of axial motion. Taking this into account, a corrective action was suggested. After corrective action, the excessive axial motion was reduced and no longer axial failure in bearing occurred.

## Data Availability

The data supporting the results of this study can be obtained upon request to the corresponding author.

## Additional Points

(i) A nonlinear dynamic model for axial motion of horizontal Pelton turbine is presented

(ii) Axial forces in the model are due to the difference between nozzle centerline and bucket centerline and due to the difference between axial position of stator and rotor magnetic field centers

(iii) Nonlinear dynamic model is used to reproduce two actual Pelton turbines axial motion

(iv) The dynamic model allows determining and evaluating the source of axial motion.

## Conflicts of Interest

The authors declare that they have no conflicts of interest regarding the publication of this paper.

## Acknowledgments

This work was supported by the University of Concepcion financial fund VRID-Enlace no. 216.094.035-1.0.

## References

[1] Y.-X. Xiao, F.-Q. Han, J.-L. Zhou, and T. Kubota, "Numerical prediction of dynamic performance of Pelton turbine," *Journal of Hydrodynamics*, vol. 19, no. 3, pp. 356–364, 2007.

[2] V. Gupta, V. Prasad, and R. Khare, "Numerical simulation of six jet Pelton turbine model," *Energy*, vol. 104, pp. 24–32, 2016.

[3] A. M. Morales B, I. F. Pachón, J. Loboguerrero U, J. A. Medina, and J. A. Escobar G, "Development of a test rig to evaluate abrasive wear on Pelton turbine nozzles. A case study of chivor hydropower," *Wear*, vol. 372-373, pp. 208–215, 2017.

[4] U. Dorji and R. Ghomashchi, "Hydro turbine failure mechanisms: an overview," *Engineering Failure Analysis*, vol. 44, pp. 136–147, 2014.

[5] M. K. Padhy and R. P. Saini, "Effect of size and concentration of silt particles on erosion of Pelton turbine buckets," *Energy*, vol. 34, no. 10, pp. 1477–1483, 2009.

[6] M. K. Padhy and R. P. Saini, "Study of silt erosion on performance of a Pelton turbine," *Energy*, vol. 36, no. 1, pp. 141–147, 2011.

[7] J. C. Chávez, J. A. Valencia, G. A. Jaramillo, J. J. Coronado, and S. A. Rodríguez, "Failure analysis of a Pelton impeller," *Engineering Failure Analysis*, vol. 48, pp. 297–307, 2015.

[8] D. Ferreño, J. A. Álvarez, E. Ruiz, D. Méndez, L. Rodríguez, and D. Hernández, "Failure analysis of a Pelton turbine manufactured in soft martensitic stainless steel casting," *Engineering Failure Analysis*, vol. 18, no. 1, pp. 256–270, 2011.

[9] M. Egusquiza, E. Egusquiza, D. Valentin, C. Valero, and A. Presas, "Failure investigation of a Pelton turbine runner," *Engineering Failure Analysis*, vol. 81, pp. 234–244, July 2017.

[10] C. Vessaz, L. Andolfatto, F. Avellan, and C. Tournier, "Toward design optimization of a Pelton turbine runner," *Structural and Multidisciplinary Optimization*, vol. 55, no. 1, pp. 37–51, 2017.

[11] A. Perrig, F. Avellan, J.-L. Kueny, M. Farhat, and E. Parkinson, "Flow in a Pelton turbine bucket: numerical and experimental investigations," *Journal of Fluids Engineering*, vol. 128, no. 2, pp. 350–358, 2006.

[12] C. Vessaz, E. Jahanbakhsh, and F. Avellan, "Flow simulation of a Pelton bucket using finite volume particle method," *IOP Conference Series: Earth and Environmental Science*, vol. 22, no. 1, Article ID 012003, 2014.

[13] C. Vessaz, *Finite particle flow simulation of free jet deviation by rotating Pelton buckets*, Ph.D Thesis, École Polytechnique Fédérale De Lausanne, Lausanne, Switzerland, 2015.

[14] C. Vessaz, E. Jahanbakhsh, and F. Avellan, "Flow simulation of jet deviation by rotating Pelton buckets using finite volume particle method," *Journal of Fluids Engineering, Transactions of the ASME*, vol. 137, no. 7, Article ID 074501, 2015.

[15] A. E. Fitzgerald and C. Kingsley, *Electric Machinery*, McGraw-Hill, New York, NY, USA, 1961.

[16] C. E. Bradford and R. G. Rhudy, "Axial magnetic forces on induction machine rotors," *Transactions of the American Institute of Electrical Engineers. Part III: Power Apparatus and Systems*, vol. 72, no. 2, pp. 488–494, 1953.

[17] J. Portos, S. Turner, and B. Veerkamp, "The influence of axial magnetic centering forces on sleeve bearing induction motors," in *Proceedings of the, IEEE Industry Applications Society-53rd Annual Petroleum and Chemical Industry Conference 2006, PCIC*, Philadelphia, PA, USA, September 2006.

[18] B. Marcusson and U. Lundin, "Axial magnetic fields, axial force, and losses in the stator core and clamping structure of a synchronous generator with axially displaced stator," *Electric Power Components and Systems*, vol. 45, no. 4, pp. 410–419, 2017.

[19] C. H. Kang, K. J. Kang, J. Y. Song, Y. J. Cho, and G. H. Jang, "Axial unbalanced magnetic force in a permanent magnet motor due to a skewed magnet and rotor eccentricities," *IEEE Transactions on Magnetics*, vol. 53, no. 11, 2017.

[20] M. Rohmer, L. San Andrés, and S. Wilkinson, "Static load performance of a water-lubricated hydrostatic thrust bearing," *Journal of Engineering for Gas Turbines and Power*, vol. 140, no. 6, Article ID 062401, 2018.

[21] M. Egusquiza, E. Egusquiza, C. Valero, A. Presas, D. Valentín, and M. Bossio, "Advanced condition monitoring of Pelton turbines," *Measurement*, vol. 119, pp. 46–55, 2018.